ACS Catalysis

pubs.acs.org/acscatalysis

Research Article

Combining Theoretical and Experimental Methods to Probe Confinement within Microporous Solid Acid Catalysts for Alcohol Dehydration

Matthew E. Potter,* Jonas Amsler, Lucas Spiske, Philipp N. Plessow, Theresah Asare, Marina Carravetta, Robert Raja, Paul A. Cox, Felix Studt, and Lindsay-Marie Armstrong

Cite This: *ACS Catal.* 2023, 13, 5955−5968

Read Online

ACCESS | Metrics & More | Article Recommendations | Supporting Information

ABSTRACT: Catalytic transformations play a vital role in the implementation of chemical technologies, particularly as society shifts from fossil-fuel-based feedstocks to more renewable bio-based systems. The dehydration of short-chain alcohols using solid acid catalysts is of great interest for the fuel, polymer, and pharmaceutical industries. Microporous frameworks, such as aluminophosphates, are well-suited to such processes, as their framework channels and pores are a similar size to the small alcohols considered, with many different topologies to consider. However, the framework and acid site strength are typically linked, making it challenging to study just one of these factors. In this work, we compare two different silicon-doped aluminophosphates, SAPO-34 and SAPO-5, for alcohol dehydration with the aim of decoupling the influence of acid site strength and the influence of confinement, both of which are key factors in nanoporous catalysis. By varying the alcohol size from ethanol, 1-propanol, and 2-propanol, the acid sites are constant, while the confinement is altered. The experimental catalytic dehydration results reveal that the small-pore SAPO-34 behaves differently to the larger-pore SAPO-5. The former primarily forms alkenes, while the latter favors ether formation. Combining our catalytic findings with density functional theory investigations suggests that the formation of surface alkoxy species plays a pivotal role in the reaction pathway, but the exact energy barriers are strongly influenced by pore structure. To provide a holistic view of the reaction, our work is complemented with molecular dynamics simulations to explore how the diffusion of different species plays a key role in product selectivity, specifically focusing on the role of ether mobility in influencing the reaction mechanism. We conclude that confinement plays a significant role in molecular diffusion and the reaction mechanism translating to notable catalytic differences between the molecules, providing valuable information for future catalyst design.

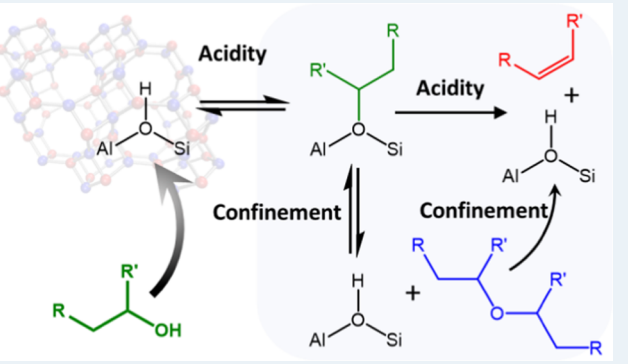

KEYWORDS: *alcohol, solid acid, heterogeneous, dehydration, porous materials, DFT, molecular dynamics*

INTRODUCTION

To fulfill future energy and chemical demands, we must investigate renewable, sustainable feedstocks.[1−6] A wide range of alternatives for these markets are being proposed with carbon utilization[7−11] and bio-based feedstocks being particularly promising.[12−15] Commercialization of the former is currently hampered by the associated costs of CO_2 capture, purification, and activation, though a significant body of work is devoted to rapidly overcoming this for future use.[10,16−18] Bio-based feedstocks contain a vast array of oxygenated products, with bioalcohols making a significant proportion of this, and offer a sustainable alcohol supply, though require water content and the presence of contaminants to be carefully addressed.[19−23] However, many other fermentation technologies and microbial methods exist that convert lignocellulose into alcohols, particularly ethanol and propanols.[24] Currently, butanol is the preferred biofuel due to its high energy density and being less corrosive than ethanol.[25−27] Despite this preference, ethanol and propanol feedstocks offer an alternative pathway to produce short-chain olefins either through direct dehydration or more complex alcohol to hydrocarbon routes.[28−31] Specifically, ethene and propene are vital precursors for the polymer, pharmaceutical, and fuel industries. At present, we rely on thermal cracking of hydrocarbons for ethene production and fluid catalytic

Received: January 24, 2023
Revised: April 6, 2023
Published: April 17, 2023

cracking for propene and butene production.[32−34] However, these processes are energy intensive and rely on fossil fuel feedstocks, making an alcohol-based dehydration route appealing.

To date, two classes of solid acid catalysts have been widely investigated for this process, alumina-based materials and microporous zeolites.[28,31,32,34−37] Alumina-based materials (typically γ-Al_2O_3) are the preferred catalyst, as they are highly stable, but they require higher temperatures (>300 °C) to maintain activity.[33,38−42] Microporous zeolites are widely used for petrochemical applications and are attractive due to tailorable product selectivity and lower reaction temperatures (200−300 °C).[43−48] These materials, with active sites located within small pores (less than 8 Å), offer significant control over a reaction. The pores themselves act as molecular sieves, allowing only smaller molecules to access the internal active sites.[49] Further once inside, the spatial constraints around the active site can dictate which transition states form and what reaction pathways are followed.[50] Finally, once formed, larger products can be trapped within the pores, near the active site, forcing further transformations to occur.[51] Diffusion of molecules to and from the active site is therefore an important feature in microporous catalysts, meaning the precise framework topology, pore diameter, and cage sizes within the material heavily influence the reactivity of the system.[48,52,53] This has been explored experimentally using a variety of characterization techniques, including one-dimensional (1D) and two-dimensional (2D) infrared spectroscopy[35,54] and solid-state NMR,[55,56] looking at identifying reactive intermediates. Along with the activity, the catalyst lifetime is also highly dependent on diffusion. Coking occurs where larger aromatic byproducts are trapped within the pores, eventually causing deactivation, or in some cases, serve as cocatalysts in the reaction.[57,58] It is the desire to control diffusion that has prompted interest in the synthesis of hierarchical materials and the development of increasingly detailed molecular dynamics simulations and combined ab initio and dynamics models to understand diffusion behavior.[59,60] This is particularly pertinent when moving toward "real systems," where pore/cage occupation can play a major role. Recent work by Cnudde et al. using *ab initio* molecular dynamics highlights this by investigating propene diffusion through a chabazite (SAPO-34) framework, where the free energy of diffusion between cages is lowered as pores become more populated with propene molecules.[48] The presence of other molecules within a pore is an important consideration when reproducing experimental systems. This is particularly poignant when considering bio-based feedstocks with significant quantities of water. Very recently, Grifoni et al. also investigated the role of water clusters in a range of zeolite species (GIS, CHA, MFI, and FAU) using metadynamics methods.[47] It was shown that water typically resides within zeolite channels, close to the acid site, with limited mobility, and the size of these species is limited in size, typically with more than three water molecules; however, it is noted that the space between water molecules can be occupied by other molecules, allowing for proton transfer to other species. Here, the role of pore confinement was used to explore the transfer of the acidic framework proton to the water cluster, confirming that it played a major role in acid site strength. Similarly, in their work on 1-propanol, Zhi et al.[29] considered the role of water on the dehydration of 1-propanol. Here, it was found that water hinders the formation of both propene and dipropyl ether, which was attributed to water-stabilizing adsorbed intermediates, therefore increasing the activation energy for a range of transformations.

Aluminophosphates (AlPOs) are structurally similar to zeolites, sharing many framework topologies, though unlike zeolites that are made of AlO_4 and SiO_4 tetrahedral units, AlPOs are made of alternating AlO_4 and PO_4 units, joined by Al−O−P bonds. AlPOs themselves are comparatively inert, however, the ability to incorporate a range of dopants into the framework leads to the formation of active sites with different functionalities.[61] Si^{4+} is among the most common dopants in AlPOs, creating silicon-doped aluminophosphates (SAPOs), where Si^{4+} can replace a P^{5+} framework atom; however, other substitution pathways can occur.[44] The resulting charge imbalance is then neutralized by a proton binding to an oxygen atom, adjacent to the Si^{4+} dopant, creating a Brønsted acid site (BAS).[44] SAPO-34 is the most widely investigated SAPO species due to its industrial implementation in the methanol-to-olefins (MTO) process.[62,63] The chabazite (CHA) framework of SAPO-34 promotes the formation of smaller propene and butene species due to the narrow pore diameters (3.8 Å), while the cages (7.3 Å in size) still allow larger aromatic molecules to form, as shown in experimental and theoretical MTO studies.[48,62,63] Further, the moderate acidity of SAPO-34 effectively activates the alcohol feedstock while limiting deactivation from the formation of heavier aromatics.[43,48,52] This makes it a good candidate for further experimental studies into alcohol dehydration and a useful model system. The Si loading in SAPO-34 is typically quite modest, with less than 10% of framework P atoms substituted by Si, meaning that the active sites are dispersed and can be considered "isolated", with limited interactions between different active sites. Further, unlike common zeolites, such as ZSM-5 or mordenite,[64,65] which have multiple distinct T-sites, SAPO-34 only possesses one crystallographic Al and P site. This makes modeling the active sites in SAPO-34 much simpler, as far fewer combinations of dopant T-site location and specific protonated oxygen need to be considered. This combined with the vast majority of Si isomorphously substituting one framework P site means the active sites in SAPO-34 are not only isolated but also uniform, making it an excellent model system to study theoretical reaction pathways.

In our previous work on ethanol dehydration, we suggested the superior ethene production of SAPO-34, over other SAPO systems, stemmed from its (comparatively) stronger BAS.[66,67] Investigating the catalytic mechanism showed that ethene is not directly formed via the monomolecular dehydration pathway in SAPO-34. Instead, diethyl ether is initially formed through a surface ethoxy species, which then decomposes into ethene, with decomposition being the rate-limiting step, with ethene formation favored at higher temperatures.[66,67] This process has repeatedly been seen through theoretical models with ZSM-5 showing ether decomposition to ethene,[68] which has also been seen in the microkinetic models of butanol dehydration by John et al. in Faujasite.[69] A preliminary quasielastic neutron scattering study observed ethene and ethanol diffusion through the SAPO-34 pore network, however, diethyl ether diffusion was not observed, suggesting that it was notably slower or just did not occur.[70] The latter result raises questions on the suitability of SAPO-34 for larger alcohol systems including propanols and butanols.

Recent theoretical work on ethanol and propanol dehydration in zeolites has begun to tackle whether confinement or acidity is the key feature. Several mechanistic steps

https://doi.org/10.1021/acscatal.3c00352
ACS Catal. 2023, 13, 5955−5968

have been explored, primarily focusing on whether the direct monomolecular formation of ethene occurs via a stepwise E_1 or a concerted E_2 elimination pathway.[71−74] Experimentally, it is challenging to distinguish between the two, however, density functional theory (DFT) studies suggest that the E_2 pathway has a lower activation barrier and is likely to be the dominant pathway.[71−74] Other studies focus on the initial binding of the alcohol to the acid site. Of particular interest is whether η^2 or a η^1 binding occurs, and whether these exist as Eigen or Zundel style complexes,[35] as this will influence which pathway is followed.[75,76] Even before this, other studies have questioned the true nature of the active site in zeolites, with recent work by Pfriem et al. focusing on the influence of water clusters on hydronium ion formation and their role in catalytic activity.[30]

In this work, we present a combined experimental and theoretical study focusing on ethanol, 1-propanol, and 2-propanol dehydration using both SAPO-34 and SAPO-5 molecular sieves. While ethene and propene production are vital areas, they will also serve as exemplar reactions to study the possibility of these catalysts being extended to larger alcohols by looking at the influence of subtle modifications to both the size and shape of the pore architecture. SAPO-5 is chosen to contrast the SAPO-34 species as the 1D channels of SAPO-5 are 7.3 Å in diameter, the same size as the cages within SAPO-34.[67] This will highlight the influence of the 3.8 Å pore windows of SAPO-34 on the alcohol dehydration. We will combine the catalytic study with molecular dynamics (MD) simulations to explore the influence of molecule size and shape on internal pore diffusion and link this back to the reaction pathways using high-level DFT quantum chemistry calculations, informing microkinetic models on the reaction itself. This will allow us to explore the influence of confinement, and acidity, of the different catalysts, extending our findings to a wider range of potential bioalcohol dehydration catalysts.

EXPERIMENTAL METHODS

Alcohol Dehydration Catalysis Methodology. Catalysis was performed using a custom-built flow reactor provided by Cambridge Reactor Design. The reactor comprised of a syringe pump, a mass flow controller, and a reactor with a heater and a control box. A 224 mm quartz reactor tube (4 mm id, 6 mm od) with a 4 mm high frit 80 mm from the base of the tube and a gas inlet 25.8 mm from the top were placed inside a heater jacket.

All catalysis was performed using a fresh 0.3 g of catalyst sieved between 300−500 μm, which, prior to reaction, was dried in the reactor at 400 °C for 1 h under a constant 29.4 mL/min flow of nitrogen. During the reaction, a carrier gas flow of 29.4 mL/min nitrogen and a mixture of 90 wt % alcohol (ethanol/1-propanol/2-propanol) and 10 wt % heptane (internal standard) were flown through the reactor, with liquid flow rates varied to give a WHSV of 1.0, 1.25, 1.50, 1.75, or 2.0 h^{-1}. Experiments were performed at either 155, 170, 185, or 200 °C for all three alcohols for both SAPO-5 and SAPO-34. Liquid feed flow rates were adjusted, so the same molar quantity of the different alcohols was used. We purposefully limited the study to these three substrates as these to demonstrate the influence of changing alcohol size, while limiting the number of possible products formed, the potential for further reactions and to ensure the reaction occurs in the vapor phase.

After 40 min on stream, 200 μL of vaporized output was injected as a gas into a PerkinElmer Clarus 400 gas chromatogram (GC) with a flame ionization detector with an HP1 cross-linked methylsiloxane (30 m × 0.32 mm × 1 μm) column. All results shown are the average of three consecutive GC injections, therefore limiting the error of our measurements, which is found to be ±3 mol %, in line with the expected GC error.

DFT and DLPNO-CCSD(T):DFT Calculations. Free energies were computed from unit cells of SAPO-34 (hexagonal: a = 13.875 Å, c = 15.017 Å) and SAPO-5 (hexagonal: a = 13.863 Å, c = 16.832 Å) with one Brønsted acid site per cell (Figure S1). Geometry optimizations were performed using plane-wave density functional theory (DFT) with a convergence criterion of 0.01 eV/Å. The Perdew−Burke−Ernzerhof (PBE) density functional[77] was employed with the D3 Grimme dispersion correction[78] as implemented in the VASP code using the standard projector-augmented waves (PAWs)[79−81] and a cutoff energy of 400 eV. The Brillouin zone was sampled at the Γ-point only[82] using Gaussian smearing with a width of 0.1 eV. Transition structures were located using automated relaxed potential energy surface scans (ARPESS),[83] and the existence of one imaginary mode connecting the correct minima of the reaction was confirmed. The harmonic approximation was applied to compute entropic contributions to the Gibbs free energy. Vibrational frequencies were derived from the partial Hessian matrix computed using a central finite difference scheme including only the adsorbate, the acid site, and its adjacent Si and Al atoms. Vibrational frequencies below 12 cm^{-1} were increased to this value because they can lead to inaccurate entropies otherwise.[84] Utilizing the hierarchical cluster model approach introduced by Sauer and co-workers,[62,85−90] the electronic energies were refined using domain-based local pair natural orbital coupled cluster (DLPNO-CCSD(T))[91−93] single-point calculations combined with complete basis set (CBS) extrapolation based on DLPNO-MP2 calculations applied to 46T cluster models of the catalyst (see eqs 1 and 2). The 46T cluster models were cut from the optimized periodic model and saturated with hydrogen atoms.[94,95]

$$E = E^{\mathrm{PBC}}_{\mathrm{PBE-D3}} - E^{\mathrm{46T}}_{\mathrm{PBE-D3}} + E^{\mathrm{46T}}_{\mathrm{DLPNO-CCSD(T)/DZ}} + \Delta E^{\mathrm{46T}}_{\mathrm{MP2/CBS}} \quad (1)$$

where

$$\Delta E^{\mathrm{46T}}_{\mathrm{MP2/CBS}} = E^{\mathrm{46T}}_{\mathrm{DLPNO-MP2/CBS}} - E^{\mathrm{46T}}_{\mathrm{DLPNO-MP2/DZ}} \quad (2)$$

In this hierarchical cluster model approach,[85−90] the cc-pVDZ basis set was used for $E^{\mathrm{46T}}_{\mathrm{DLPNO\text{-}CCSD(T)/DZ}}$ of the 46T cluster model. $\Delta E^{\mathrm{46T}}_{\mathrm{MP2/CBS}}$ represents the difference between MP2-based CBS extrapolation ($E^{\mathrm{46T}}_{\mathrm{DLPNO\text{-}MP2/CBS}}$) and MP2/cc-pVDZ calculations for 46T clusters ($E^{\mathrm{46T}}_{\mathrm{DLPNO/DZ}}$). The CBS extrapolations of Hartree−Fock energies were carried out with the three-point exponential formula[96] with cc-pVXZ (X = D, T, Q). The MP2 correlation was extrapolated using the two-point formula[97] with cc-pVXZ (X = D, T). PBE-D3 calculations on 46T cluster models were performed using the VASP with a vacuum of more than 16 Å separating periodic images of the structure. The ORCA software package[98,99] was used to perform DLPNO-CCSD(T),[93] DLPNO-MP2,[100−102] and restricted Hartree−Fock (RHF) calculations for cc-pVXZ (X = D, T, Q)[103] in the DLPNO approximation.[93,104−106] The

https://doi.org/10.1021/acscatal.3c00352
ACS Catal. 2023, 13, 5955−5968

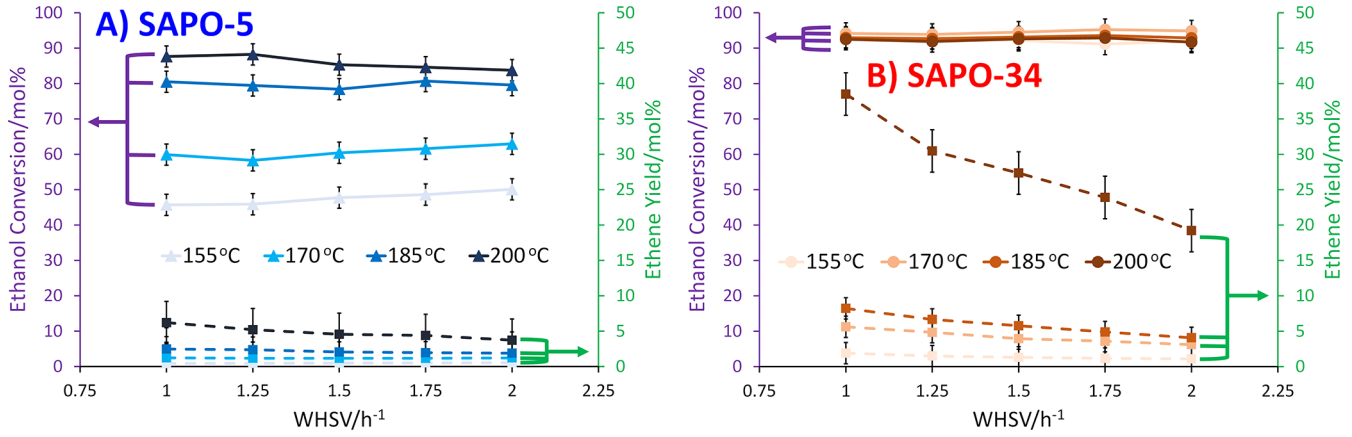

Figure 1. Ethanol dehydration catalytic data comparing (A) SAPO-5 and (B) SAPO-34, showing ethanol conversion and ethene yield, varying with temperature and WHSV.

RIJCOSX (resolution of identity for Coulomb integrals and seminumerical chain-of-sphere integration for HF exchange integrals) approximation[107] with GridX6 was used in RHF calculations. Parts of the calculations were operated using the atomic simulation environment.[108]

Molecular Dynamics. Molecular dynamics calculations were performed using the COMPASS II forcefield[109] within the Materials Studio package.[110] Simulation boxes of 2 × 2 × 5 and 3 × 3 × 3 unit cells were employed for SAPO-5 (AFI) and SAPO-34 (CHA), respectively, with Si substituted for P atoms at random locations. The temperature used was 428 K. All atoms were free to move during the simulations. Simulations were performed for two million time steps, where each time step was 10^{-15} s, giving a total simulation time of 2 nanoseconds. RMS displacement calculations were performed on the final 1 ns of data.

Microkinetic Modeling. Microkinetic modeling was performed using the *surfprobe* program of the DETCHEM software package[111] at a reference pressure of 1 bar. To ensure convergence of the steady states, coverages are evaluated after 10^4 s. To convert the surface fluxes to TOFs, a surface coverage of 10^{-4} mol/cm^2 has been chosen. Further details are given in the Supporting Information (SI).

RESULTS AND DISCUSSION

Confirming Catalyst Integrity. As per our previous work, SAPO-34 and SAPO-5 were successfully synthesized.[66,70,112] The characterization and physicochemical results (Figures S2−S5 and Tables S1−S3) were in excellent agreement with our previous work, so we refer the reader to these works for a more in-depth discussion of the characterization and acidic properties. Importantly, in both cases, the intended framework (SAPO-34, CHA; SAPO-5, AFI) was the only crystallographic phase detected, showing the phase purity of the systems (Figure S2). Surface areas obtained from nitrogen physisorption (Figure S3) were in line with expected values for these systems and the isotherm shape, and micropore volumes obtained confirmed that both species were primarily microporous (Table S1).[66,70,112] ^{27}Al and ^{31}P NMR confirmed that Al(OP)$_4$ and P(OAl)$_4$ were the main signals, as expected (Figures S4A,B). ^{29}Si NMR (Figure S4C) and the metal loadings (Table S2) confirmed that a significant amount of Si(OAl)$_4$ species were present in SAPO-34, whereas silicon islands had formed within the SAPO-5 framework, as seen by the signal at −97 ppm, attributed to Si(OSi)$_2$(OAl)$_2$ species, likely from 5- and 8-silicon islands, that are known to create BAS.[66,70,112] This led to SAPO-34 having a greater number and stronger BAS than SAPO-5, as shown by NH_3 temperature-programmed desorption (NH_3-TPD; Figure S5 and Table S3). Previously, we have seen no evidence of Lewis acidity in these species, in line with other literature reports. Therefore, both frameworks were successfully synthesized. We can assume that due to the difference in framework topologies, SAPO-5 will be a less confined system, with the smaller pore windows of SAPO-34, making it a more confined system for catalysis to occur in.

Ethanol Dehydration. SAPO-5 and SAPO-34 were tested at WHSVs between 1.0 and 2.0 h^{-1} over a temperature range of 155 to 200 °C (Figures 1 and S6−S8). At the lower temperature range of 155 °C, SAPO-5 achieves modest activity, with conversion ranging between 45−50 mol % (Figure S6A). At this temperature, SAPO-5 is almost exclusively producing diethyl ether (Figure S6B), with a maximum ethene selectivity of 2 mol % (Figures 1A and S6C). Changes in WHSV at this temperature only subtly influence the reactivity (Figures 1A and S6). This is due to the benefits of the increased ethanol concentration being negated by the larger total flow rate and this lower contact time. At 200 °C, SAPO-5 reaches a higher ethanol conversion between 84 and 88 mol % (Figures S6A and S8) due to improved activity from higher temperatures. Diethyl ether is still the primary product (selectivity between 87−91 mol %, Figure S6B), but greater quantities of ethene are also formed (9−13 mol %, Figures 1A, S6C, and S8). No other products were seen likely due to the mild temperatures used. Thus, increasing the temperature increases the ethene selectivity, in line with our previous observations.[66,67]

Compared to larger-pored SAPO-5, the smaller-pored SAPO-34 shows increased activity (Figures 1B, S7, and S8). Across the whole temperature and WHSV range, the ethanol conversion remained between 91−95 mol % (Figures S7A and S8). The ethanol conversion for SAPO-34 remains constant, despite changes in operating parameters, suggesting that this is not a kinetic effect. Recent works suggest that this could be due to our conditions, where SAPO-34 only is approaching equilibrium conversion for ethanol dehydration,[113] and agree with our findings that lower temperature favors diethyl ether formation, before this subsequently forms ethene, and this may also be due to nonoptimized reactor design or catalyst packing

https://doi.org/10.1021/acscatal.3c00352
ACS Catal. 2023, 13, 5955−5968

within the fixed bed.[114] In our previous works, the activation energies of three possible reaction steps were found to be between 66 and 143 kJ/mol, under similar conditions, as those employed here. These values are orders of magnitude higher than what would be expected for pore diffusion processes, suggesting that the system is not pore diffusion limited. Similarly, the estimated Weisz−Prater criterion for our system is 2.7×10^{-5} (see SI for calculation), which is significantly below 1, signifying that this process is also not mass-transport-limited; thus, we are in a reaction limited regime, and thus, our experiments are kinetically limited with minimal contributions from diffusion limitations. Unlike SAPO-5, changes in WHSV noticeably influence the catalytic behavior of SAPO-34, namely, the product selectivity, where larger WHSV favoring diethyl ether formation and smaller WHSV favoring ethene, something highlighted in the 200 °C data (Figure 1B). In our previous work, we suggest that diethyl ether formation is a second-order process with respect to ethanol; thus, increasing the WHSV leads to greater ethanol concentration and increased diethyl ether formation. We do not see such behavior in SAPO-5, likely due to the larger pore of SAPO-5, facilitating more interactions between ethanol molecules within the pore; thus, diethyl ether formation is already accelerated.

The increased activity of SAPO-34 over SAPO-5 (Figure S8) is likely due to a combination of acidity and confinement factors. NH_3-TPD confirms that SAPO-34 has almost five times the number of BAS than SAPO-5, but SAPO-34 also has a stronger BAS (Figure S5 and Table S3). Also, one of the fundamental principles of microporous catalysis is that by being confined, lower reaction activation barriers are achieved. This has repeatedly been shown in DFT and combined QM:MM studies, where the van der Waals and dispersion forces from pore confinement lower the activation energy.[34] As an extension, it is likely that the larger-pore SAPO-5 will stabilize the ethanol transformation to a lesser extent than the smaller SAPO-34 species. Therefore, there are several factors that will be contributing to the improved activity of SAPO-34 over SAPO-5 (Figure S8).

Focussing on the products formed in SAPO-34 (Figures 1B and S7B), we see that at low temperatures (155 °C), the diethyl ether selectivity ranges from 92 to 95 mol % for all WHSVs studied, making it the dominant product (Figure S7B). However, increasing the reaction temperature to 200 °C shows an increase in ethene selectivity to between 35−59 mol % (Figure S7C, again no other products were seen). In our previous work, we attributed this to the sequential reaction pathway of ethanol forming diethyl ether, which then decomposes to ethene, with the latter step being rate limiting, causing a build-up of diethyl ether.[66,67] Increasing the temperature increases the rate of ether decomposition, leading to more ethene. We also note that other studies have also come to similar conclusions by considering ethene and diethyl ether formation as parallel competing reactions, both directly forming from ethanol.[39,115] The improved ethene selectivity of SAPO-34 compared to SAPO-5 (Figure S8) again is likely the combination of confinement and acidity effects, which we explore through a combined DFT/MD study.

Brønsted acid-catalyzed dehydration pathways were calculated using the hierarchical cluster model approach described in DFT and DLPNO-CCSD(T):DFT calculations section. The considered mechanism for ethanol dehydration according to Figure 2 includes the formation of ethene and diethyl ether

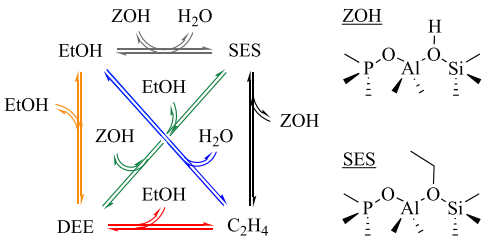

Figure 2. Suggested dehydration mechanism for the formation of ethene and diethyl ether (DEE) from ethanol (EtOH). The surface ethoxy species (SES) is the intermediate along the stepwise paths, whereas the concerted paths in orange, blue, and red circumvent SES formation. Adapted from Amsler et al., ref 72, with permission from the Royal Society of Chemistry.

from ethanol through concerted and stepwise pathways. Stepwise pathways begin with the formation of surface ethoxy species (SES) in the first step.[72] An analogous mechanism was assumed for dehydration of 1-propanol to dipropyl ether, propene, and surface propoxy species (SPS).

The calculated Gibbs free energy barriers for ethanol dehydration in SAPO-5 and SAPO-34 at 473.15 K and at a reference pressure of 1 bar are shown in Figure 3. The transition structures of the most important elementary steps are depicted above the free energy diagrams. We have chosen here to focus on a SAPO-34 and SAPO-5 system with identical substitution mechanisms, despite this not being the main site in SAPO-5. This was done to limit the number of variables and explore the influence of confinement on the activation energies.

Alcohol dehydration to the ether or alkene starts with adsorption of ethanol at the acid site of the catalyst, with a computed Gibbs free energy of adsorption of −14 kJ/mol in both SAPO-5 and SAPO-34. Hydrogen bonds of the activated complexes to the framework oxygen atoms are more easily formed in SAPO-34 and often shorter than in SAPO-5 due to beneficial confinement. SES formation is a prominent example (Figure 3, gray box), where the water molecule can form two hydrogen bonds of 2.0 Å to the SAPO-34 framework in a chelate-like coordination. A similar two-fold coordination site was not found in SAPO-5, leading to a less stabilised transition state and a higher energy barrier. Unsurprisingly, the transition structures are thus generally less stabilized in the larger SAPO-5 pores. Except for diethyl ether formation from SES (green; 113 kJ/mol), all energy barriers are higher than in SAPO-34, pointing to SAPO-5 being a less active material. Among the adsorbed species (ZOH*), water is more stable on SAPO-34, whereas diethyl ether is more stable on SAPO-5, see also Table S4.

The stepwise reaction paths (Figure 3, gray/green, gray/black) *via* SES to ethene or diethyl ether are clearly preferred in SAPO-34, compared to the concerted (direct) paths from adsorbed alcohol (Figure 3, orange, blue). In SAPO-5, however, the higher barrier of 165 kJ/mol for SES formation (gray) makes concerted diethyl ether formation (Figure 3, orange, 153 kJ/mol) the preferred pathway. Ethene would then be formed upon stepwise diethyl ether decomposition *via* SES. This suggests that the SES is a vital part of the SAPO-34 ethanol dehydration pathway, whereas SAPO-5 likely favors the concerted pathway to the ether.

Comparing the barriers of diethyl ether and ethene formation from SES in SAPO-5 (Figure 3, green and black, respectively) shows that the ether is significantly favored

https://doi.org/10.1021/acscatal.3c00352
ACS Catal. 2023, 13, 5955−5968

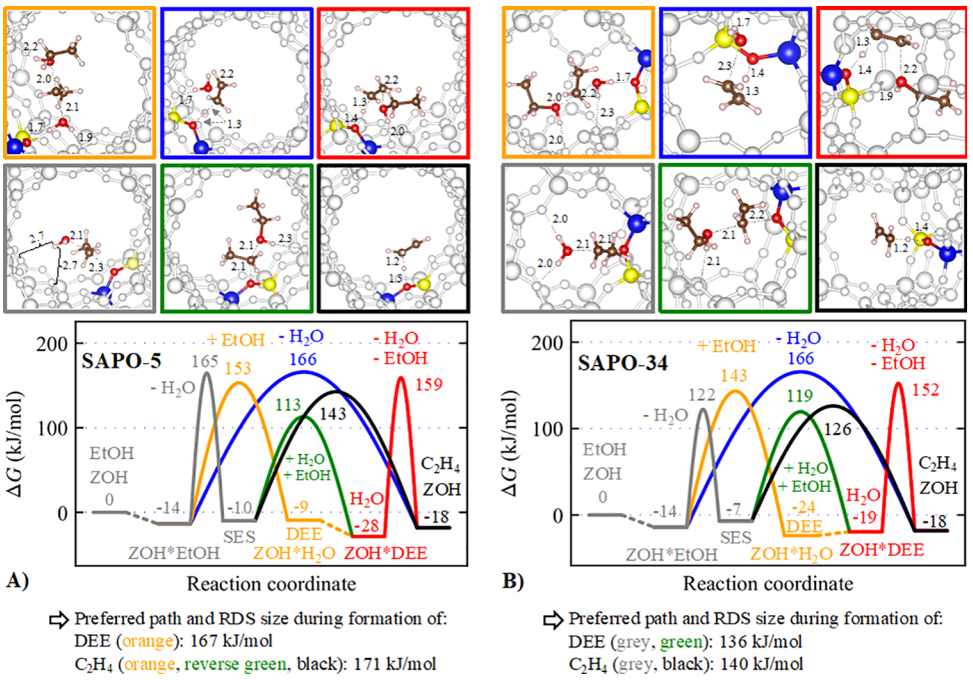

Figure 3. Free energy barriers of ethanol dehydration for (A) SAPO-5 and (B) SAPO-34 at 473.15 K and at a reference pressure of 1 bar. Transition structures with distances in Å are depicted above the diagrams, the rate-determining steps (RDS) are extracted below. The values for the barriers in the preferred path analysis were determined using the energy span model that is measured from the lowest adsorbed state to the highest barrier. The atoms are color coded, such that brown = carbon, pink = hydrogen, red = oxygen, yellow = aluminum, blue = silicon.

kinetically (113 v 143 kJ/mol). This supports the experimental observation that diethyl ether formation is heavily favored in SAPO-5. Note that the SES-mediated stepwise diethyl ether decomposition to ethene (Figure 3, reverse green, then black) is preferred over the concerted path (red) in both catalysts. Relative to adsorbed diethyl ether (ZOH*DEE), the barriers are 171 kJ/mol in SAPO-5 and 145 kJ/mol in SAPO-34, explaining the low ethene formation in SAPO-5. In contrast, the concerted formation of diethyl ether and ethene from the SES in SAPO-34 (Figure 3, green and black, respectively) shows that ether formation is still favored (119 v 126 kJ/mol), though not as significantly. Thus, the diethyl ether selectivity in SAPO-34 should be more sensitive to ethanol partial pressure than in SAPO-5 at identical conversions, which, for the low pressures applied, could also explain the greater yields of ethene seen (Figures 1 and S8). Using microkinetic modeling, it has been found that for ethanol dehydration in SAPO-34, an increase in temperature from 155 to 200 °C results in an increase of the alkene/ether ratio by a factor of over 100 (see Table S5); this is solidified by the experiment (Figure 1B), which show a drastic increase in ethylene selectivity at higher temperatures. For ethanol dehydration on SAPO-5, a smaller increase of the alkene/ether ratio was calculated (factor 20), which is substantiated by the experimental results in Figure 1A. At higher temperatures, the formation of alkenes is thermodynamically favored. The values calculated here are in good agreement with similar studies, albeit using different materials and reaction temperatures. Alexopoulos et al. calculated an energy barrier of 118 kJ/mol for SES formation at 500 K in ZSM-5, and suggested, as we do, that higher temperatures and lower ethanol partial pressure favor ethene formation.[68] Similar work by Roy et al.,[116] on an γ-Al_2O_3 surface, focusing on Lewis acidity found the experimental activation energy for ethanol to ethylene to be 145 kJ/mol, which compares well with our values (Figure 3).

While the calculated reaction energetics (Figure 3, green and black lines) suggest that diethyl ether should decompose to ethene more readily in SAPO-34 than SAPO-5 (see above), we also investigate the mobility of diethyl ether within these frameworks. Molecular dynamics (MD) simulations (Figure 4)

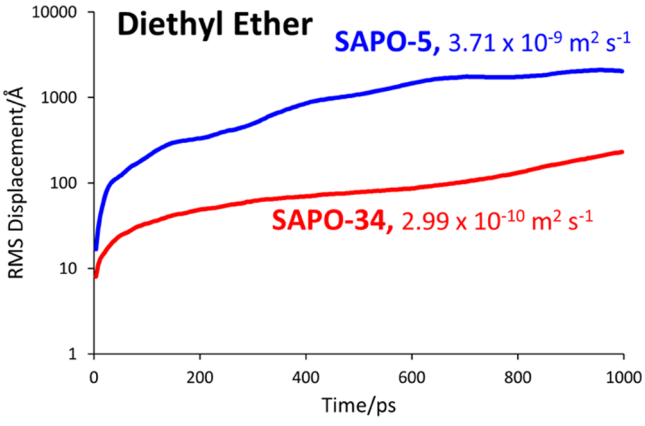

Figure 4. Simulated RMS displacement plots comparing the relative motion of diethyl ether within SAPO-5 (AFI) and SAPO-34 (CHA) frameworks at 428 K, with diffusion coefficients annotated.

show, as expected, that diethyl ether is significantly more mobile (nearly 10 times the RMS displacement) within the larger 7.3 Å pore of the SAPO-5 (AFI) framework (diffusion coefficient of 3.71×10^{-9} m^2 s^{-1}) than within the smaller 3.8 Å pore windows of the SAPO-34 (CHA) framework (2.99×10^{-10} m^2 s^{-1}). This means diethyl ether will reside considerably longer within the CHA system, near active sites allowing far more opportunities for a catalyzed decomposition

https://doi.org/10.1021/acscatal.3c00352
ACS Catal. 2023, 13, 5955−5968

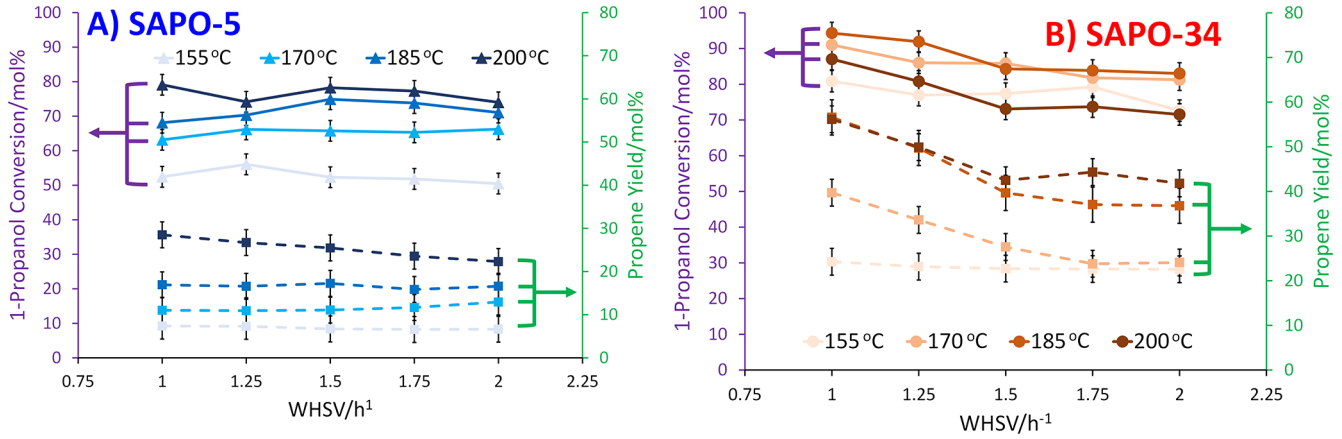

Figure 5. 1-Propanol dehydration catalytic data comparing (A) SAPO-5 and (B) SAPO-34, showing 1-propanol conversion and propene yield varying with WHSV and temperature.

reaction to ethene to occur, increasing the ethene selectivity in SAPO-34, while reducing the diethyl ether selectivity. Indeed, we see that this behavior is not exclusive to diethyl ether, as ethanol and ethene both diffuse far more slowly through SAPO-34 (Figure S9; 2.81×10^{-11} and 1.08×10^{-9} m^2 s^{-1}, respectively) than SAPO-5 (Figure S9; 6.19×10^{-9} and 7.41×10^{-8} m^2 s^{-1}). We note that in SAPO-34, unlike in SAPO-5, ethanol diffuses more slowly than diethyl ether (Figure S9). Despite being smaller than diethyl ether, ethanol will experience greater hydrogen bonding with acid sites due to the hydroxy functional group, which may hinder diffusion through the pore. SAPO-34 has stronger acid sites than SAPO-5, meaning that there would be stronger interactions with ethanol in the SAPO-34 system, anchoring ethanol. Further, the larger pore of SAPO-5 would mean that if ethanol detached from the acid site, it could diffuse away through the channel. However, in SAPO-34, the smaller pore forces ethanol to remain close to the acid site promoting reattachment and thus slower diffusion. In contrast, the weaker hydrogen bonding of SAPO-5 with ethanol and the more spacious pore mean that ethanol can diffuse more freely than diethyl ether.

To better distinguish between the influence of confinement and active site, we now expand our catalytic study to include 1-propanol and 2-propanol feedstocks. As ethanol and the propanols (and associated products) are all much smaller than the SAPO-5 pore, the confinement effects should be similar for all species with this catalyst. However, we would expect a greater influence of confinement for ethanol and the propanols in SAPO-34. We note that changing the alcohol feedstock will not alter the active sites in SAPO-5 or SAPO-34; therefore, the effect of acidity should be constant. Thus, changing the alcohol feedstock should highlight just the influences of confinement between the two SAPOs.

1-Propanol Dehydration. At the range of temperatures studied (155−200 °C), SAPO-5 shows similar activity with 1-propanol and ethanol (Figures 5A and S10). Specifically, at 155 °C, the 1-propanol conversion is between 50−56 mol %, compared to 74−79 mol % at 200 °C, spanning the same range as the ethanol data (Figures S6A and S10A). As both ethanol and 1-propanol are primary alcohols, the C_3 chain should have a greater positive inductive effect than the C_2 chain, helping to activate the molecule. As before, we see that increasing the reaction temperature increases conversion (Figures 5 and S10A).

There is significantly more alkene forming in SAPO-5 with the 1-propanol feedstock than when ethanol is used (Figures 1A and 5A). At 155 °C, propene selectivity varies between 23−30 mol %, rising to between 47−53 mol % at 200 °C, depending on the WHSV used (Figure S10C). However, we note, like the ethanol case (Figure 1), varying the WHSV has little influence on the catalytic performance of SAPO-5. The improved alkene selectivity and reduced ether formation (compared to ethanol; Figures S6 and S10) are likely due to the longer carbon chain lowering the activation energy of propene formation, compared to ethene. It is unclear whether this is due to faster dipropyl ether decomposition or the direct unimolecular dehydration of 1-propanol to propene occurring at a faster rate. To further investigate this, microkinetic modeling has been performed to investigate the influence of the reaction barrier for the green and black pathways of Figure 8 on the alkene/ether ratio; results of this are shown in Table S6. We see that variation of the black barrier has a far greater impact on the alkene/ether ratio than the variation of the green barrier does, showing us a clear preference for the black pathway for production of the alkene.

Despite the variations in temperature, SAPO-34 has lower conversions with 1-propanol (72−94 mol %, Figure S11A) than with ethanol (91−95 mol %, Figure S7A) as the feedstock, despite the 1-propanol expected to be more active for this reaction than ethanol. We reason that this reduced activity is due to confinement effects, where the smaller-pored SAPO-34 may struggle to accommodate larger reaction intermediates and transition states, compared to SAPO-5 (Figures 3 and S12). Despite this reduced activity, SAPO-34 is still more active than SAPO-5, showing greater activity, under identical reaction conditions (Figure S12). Like SAPO-5, SAPO-34 typically favors propene over dipropyl ether. Thus, moving from ethanol to 1-propanol reduces the activity of SAPO-34 but increases total alkene production (Figures S8 and S12). These findings suggest that either diffusion of 1-propanol to the active sites is being hindered or is harder to activate within the SAPO-34 pores or a combination thereof. An analogous prediction of the Gibbs free energy barriers for 1-propanol under the same reaction conditions in SAPO-34 is shown in Figure 6. Given the variety of active sites present in the SAPO-5 system, we have not performed an analogous DFT

https://doi.org/10.1021/acscatal.3c00352
ACS Catal. 2023, 13, 5955−5968

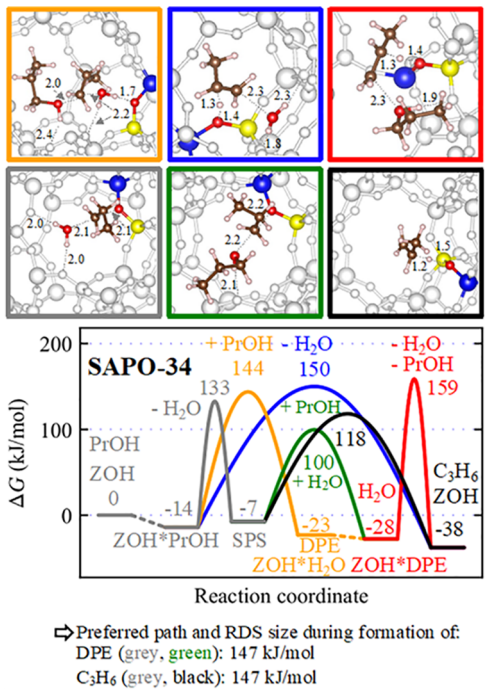

Figure 6. Free energy barriers of 1-propanol (PrOH) dehydration for SAPO-34 at 473.15 K and a reference pressure of 1 bar. Transition structures with distances in Å are depicted above the diagram, the size of the rate-determining step (RDS) is extracted below. The atoms are color coded such that brown = carbon, pink = hydrogen, red = oxygen, yellow = aluminum, blue = silicon.

study for SAPO-5; instead, we chose to focus on the influence of changing substrate size, transitioning from ethanol to 1-propanol in SAPO-34.

Going from an ethanol to a 1-propanol feedstock in SAPO-34 increases the energy barrier for forming the surface alkoxy species (Figures 3 and 6) from 122 to 133 kJ/mol—the first barrier in the stepwise alcohol dehydration path (147 kJ/mol relative to adsorbed 1-propanol) to propene is now higher than the second one. Roy et al. suggested that on a nonporous γ-Al_2O_3 surface, where confinement does not play a significant role,[116] the activation energy from ethanol to 1-propanol would decrease from 145 to 141 kJ/mol. This shows that, in SAPO-34, the SPS is less readily formed than the SES, likely due to spatial constraints within the smaller SAPO-34 pore. We have calculated a 31 kJ/mol difference in dispersive interaction for SAPO-5 compared to SAPO-34, which is in line with the fact that SAPO-5 has a larger pore and therefore smaller dispersive interactions.[117] Despite this increase in energy, the SPS is still the preferred pathway for alkene and ether formation (Figure 6). The greater energy barrier for 1-propanol, compared to ethanol, aligns with the lower catalytic activity seen (Figures 1 and 5). It is noteworthy that the surface alkoxy route (Figures 3 and 6, gray) increases from 122 to 133 kJ/mol for SAPO-34 from ethanol to 1-propanol. Likely this is due to the smaller substrate being less sterically hindered within the smaller-pored SAPO-34, therefore lowering the activation barrier of the process. The concerted alkene formation (Figures 3 and 6, blue) decreases from 166 to 150 kJ/mol. This minor stabilization would be expected as 1-propanol has slightly larger dispersion interactions compared to ethanol (we calculated a difference of 9.8 kJ/mol from D3). In addition, the alkene is strongly favored in the equilibrium of dipropyl ether (DPE) and propene. Extrapolating this trend further to bulkier reagents would likely see that the concerted alkene formation plays a greater role, potentially becoming the favored pathway. Dispersion interactions mainly depend on the number of adsorbate atoms (Figure S13), as has also been observed in the literature.[117] Our computational findings are in good agreement with previous literature, particularly from Zhi et al., who focussed on 1-propanol dehydration within the ZSM-5 catalyst. At 433 K, they calculated a value of 136 kJ/mol for propoxide dehydration to propene, whereas our smaller-pored SAPO-34 system has a lower value of 118 kJ/mol, likely due to a combination of the smaller pore size and higher temperatures studied.

In summary, kinetic selectivity for ether or alkene can be explained by the free energy barriers (green, black) in the stepwise paths. Figures 3 and 6 illustrate the relations between these barriers relative to the adsorbed alcohol. The largest difference is clearly observed for ethanol dehydration in SAPO-5 with a preference of 30 kJ/mol toward diethyl ether. The difference is only 7 kJ/mol for ethanol dehydration in SAPO-34 and 18 kJ/mol for 1-propanol dehydration in the same catalyst. An experimentally observed selectivity toward propene can only be explained if DPE stays sufficiently long in vicinity to the active site, or visits multiple sites, allowing it to decompose according to the thermodynamic equilibrium.

Again, comparing the diffusion of dipropyl ether in the two SAPO systems shows that it diffuses far more rapidly through SAPO-5 (3.79×10^{-10} m^2 s^{-1}) than SAPO-34 ($<1.00 \times 10^{12}$ m^2 s^{-1}), differing by an order of magnitude (Figure 7). This

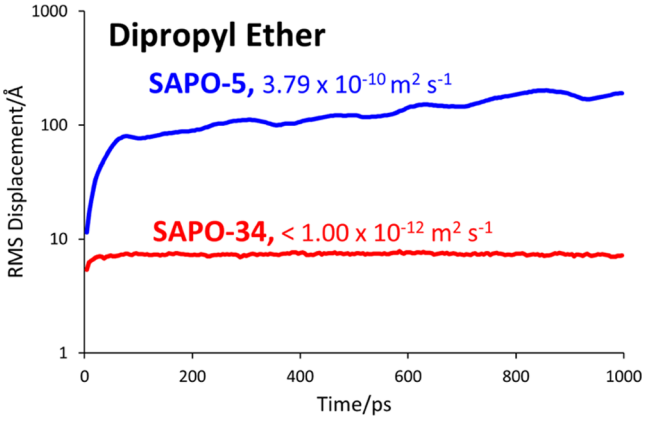

Figure 7. Simulated RMS displacement plots comparing the relative motion of dipropyl ether within SAPO-5 (AFI) and SAPO-34 (CHA) at 428 K, with diffusion coefficients annotated.

suggests that while the ether to alkene step has the largest energy barrier of the 1-propanol SAPO-34 pathway (Figure 6), there will be greater opportunities for it to occur, whereas the propene can diffuse out of the pores far more rapidly (Figure S14). This will lead to greater selectivity to propene and less selectivity to dipropyl ether.

2-Propanol Dehydration. At lower temperatures (155 °C), SAPO-5 achieves similar levels of conversion with 2-propanol (Figure S15), as with 1-propanol (Figure S10) and ethanol (Figure S6). However, at elevated temperatures (200 °C) and a lower WHSV (1.0−1.5 h^{-1}), it reaches near-quantitative conversion (Figure S15A). This improved activity at higher temperatures is due to the superior activity of secondary (and tertiary) alcohols, compared to primary

https://doi.org/10.1021/acscatal.3c00352
ACS Catal. 2023, 13, 5955−5968

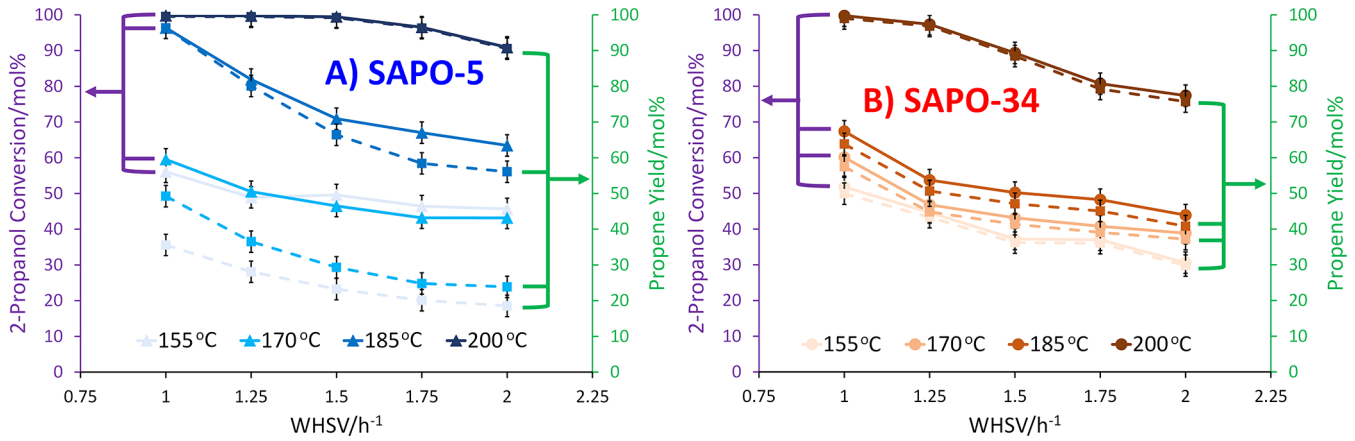

Figure 8. 2-Propanol dehydration catalytic data comparing (A) SAPO-5 and (B) SAPO-34, showing the propene selectivity varying with WHSV and temperature.

alcohols for dehydration reactions. Again, alcohol conversion drastically increases at higher temperatures, with significant jumps in activity seen between 170 and 200 °C (Figure S15A).

Considering the product distribution of SAPO-5 with 2-propanol (Figures 8 and S15B), greater preference is shown for alkene formation, more so than with ethanol and 1-propanol (Figures 8 and S16). This is shown by propene now being the dominant product under all studied conditions, with propene selectivity ranging from 58−78 mol % at 155 °C to above 98 mol % at 200 °C (Figure 8). Thus, here, changing between ethanol and 2-propanol results in increased activity and alkene formation for SAPO-5. Unlike in the ethanol and 1-propanol cases, varying the WHSV significantly affects the catalytic performance (Figure 8A) of SAPO-5. This suggests that the alcohol interactions within the pore are becoming hindered, as we saw in the SAPO-34 system, and thus WHSV, and therefore, alcohol concentrations are beginning to influence activity.

Despite possessing a far greater number and stronger BAS, the activity of SAPO-34 for 2-propanol dehydration is comparable to SAPO-5, and at low temperatures (155 °C), SAPO-5 has become the more active catalyst (Figures 8, S17, and S18). At 155 °C, SAPO-34 has a 2-propanol conversion of between 32−51 mol % (Figure S17A), compared to SAPO-5 (46−56 mol %; Figure S16A). This is a significant finding, showing that SAPO-34 is noticeably less effective at converting 2-propanol than 1-propanol or ethanol, though despite SAPO-34's lower activity with 2-propanol, propene is almost exclusively formed (Figures 8B, S17B, and S18), showing a strong preference for alkene formation. The low quantities of diisopropyl ether suggest the following: (1) If a parallel competitive mechanism is occurring, then ether is not being formed, likely due to the steric constraints of the bulky ether, as suggested above, or, once formed it cannot leave the pores. (2) If the sequential mechanism is happening, the ether is being formed but is consumed so fast that it is in a pseudo-steady state, with no build-up. This would support the idea that the ether becomes trapped in the pores of SAPO-34 and is forced to react further to propene before leaving the pores (product selectivity).[51]

Comparing the behaviors of the SAPO-5 and SAPO-34 systems with 2-propanol as a feedstock, we see that the larger-pored SAPO-5 has a higher conversion but lower propene selectivity (Figure S18). Again, comparing the diffusion of the bulkier diisopropyl ether through the SAPO-5 and SAPO-34 pores (Figures 9 and S18; 3.00×10^{-10} and $<1.00 \times 10^{-12}$ m^2 s^{-1}, respectively) confirms our theory above that indeed the ether can diffuse far more readily out of SAPO-5, whereas it is far less mobile in SAPO-34, leading to improved decomposition to propene. We note that the reaction mechanism likely differs between primary (ethanol and 1-propanol) and secondary alcohols (2-propanol); however, the pathway and possible routes are expected to be the same for SAPO-5 and SAPO-34 and will be influenced by the larger substrate, allowing us to draw comparisons from our kinetic findings. Previous work by Gunst et al.[118] has compared the activity of alcohol isomers, namely, 1-butanol and iso-butanol with ZSM-5, concluding that iso-butanol favors direct dehydration to iso-butene, while 1-butanol favors ether formation. We envisage that a similar trend, in line with our catalytic data, would apply to the mechanism of 1-propanol and 2-propanol.

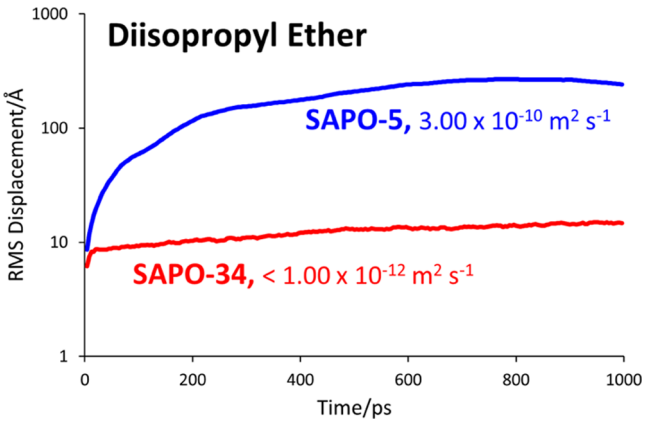

Figure 9. Simulated RMS displacement plots comparing the relative motion of diisopropyl ether within SAPO-5 (AFI) and SAPO-34 (CHA) at 428 K, with diffusion coefficients annotated.

Overall, combining our catalysis and quantum chemical and molecular dynamics findings (Table 1), we see a trend where SAPO-34 is becoming increasingly inactive, as the substrates get larger. We believe that this is due to a combination of an increase of the formation barrier for the surface alkoxy species, which is entropy related, slowing down the reaction, and the more hindered pore diffusion of the alcohol substrates, preventing the substrate reaching the active sites (Figure 10).

https://doi.org/10.1021/acscatal.3c00352
ACS Catal. 2023, 13, 5955−5968

Table 1. Summarizing the Key Findings Relating to Catalysis, Quantum Chemical Calculations, and Molecular Dynamics Simulations

		catalytic data (mol %)[a]		calculated energy barrier (kJ/mol)[b]		RMS displacement (Å)[c]	
catalyst	alcohol substrate	alcohol conversion	alkene selectivity	alkene formation	ether formation	alcohol	ether
SAPO-5	ethanol	51	2	171	167	3184	2040
	1-propanol	50	24	N/A	N/A	3591	191
	2-propanol	46	58	N/A	N/A	6073	241
SAPO-34	ethanol	92	5	140	136	12	231
	1-propanol	73	48	147	147	13	7
	2-propanol	31	99	N/A	N/A	11	15

[a]Catalytic data represents the values at 155 °C, with a WHSV of 2 h^{-1}. Values shown are the composition of the molecules in the outlet stream. [b]Highest energy values for the lowest energy pathway. [c]Values after 1000 ps.

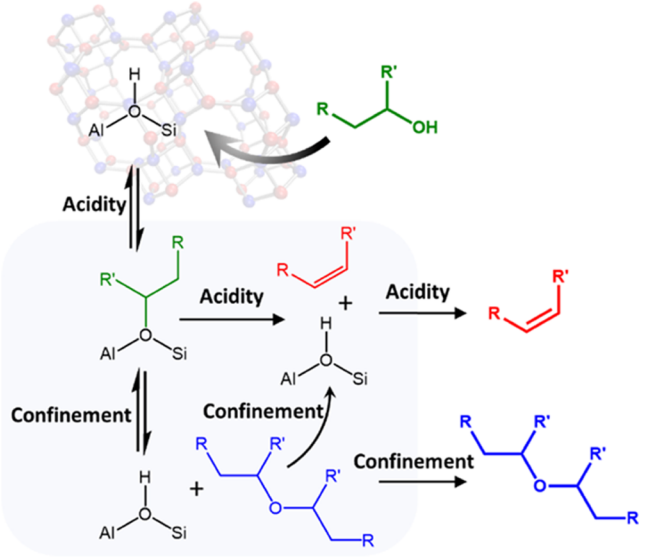

Figure 10. Schematic showing the proposed mechanism of alcohol dehydration. Confinement will influence the diffusion to and from active sites and the energy barriers, whereas acidity will determine the product selectivity and overall activity.

Through this study, we believe we have successfully distinguished between acidity effects (ethanol) and confinement effects (2-propanol) for the two SAPO systems. This will aid future design of alcohol dehydration catalysts for a much wider range of alcohol substrates, including bio-based alcohols.

CONCLUSIONS

Alcohol dehydration is an appealing route toward the sustainable production of short-chain alkenes. Designing optimal catalysts for the selective formation of alkenes requires detailed knowledge of the alcohol dehydration pathway, pore diffusion, and the influence of confinement and acidity. To understand these different factors, we have explored the behavior of two SAPO systems, the larger-pored SAPO-5 and the smaller-pored SAPO-34, for the dehydration of ethanol, 1-propanol, and 2-propanol. In doing so, the acidity influence is kept constant within the framework structure, while the confinement effects are varied, and we investigated combining experimental catalysis data, with theoretical quantum chemical data to calculate reaction energy barriers and molecular dynamics simulations to explore pore diffusion.

Our catalytic study showed that changing the alcohol substrate had a significant influence on the behaviors of the two systems. When ethanol was used as a substrate, confinement would play a minimal role, and therefore, SAPO-34 proved to be more active than SAPO-5, with greater selectivity to the alkene. Progressing to 1-propanol and then 2-propanol, we saw the activity of SAPO-34 drop, eventually matching the activity of SAPO-5. Further, despite the reduced activity, SAPO-34 transitioned to exclusively forming the alkene product, with scarce little ether being formed. These observations were investigated through a DFT study. This concluded that, as the substrate increased in size, the energy barrier for the activation of the alcohol to a surface alkoxy species also increased in SAPO-34, explaining the reduced activity. Compared to ethanol dehydration in SAPO-34, a bypassing of ether formation is likelier during 1-propanol dehydration due to a decreased barrier for the concerted pathway. Thus, the experimentally observed selectivity toward propene can only be explained if the ether is sufficiently immobile to be decomposed toward the thermodynamic equilibrium.

Molecular dynamics repeatedly showed that the ether product diffused far more readily in the SAPO-5 framework than SAPO-34, where it was quite immobile. The increased residency time of the ether, especially compared to the alkene, is likely a key factor in the improved alkene selectivity of SAPO-34. Extending the length of time, the ether spends inside the framework offers more opportunities for ether decomposition into the desired alkene product, which could allow the alkene to be selectively formed at much lower temperatures.

Overall, our approach of combining high-level quantum chemical calculations, MD simulations, and the gathering of detailed catalytic data provided complimentary insights for the design of solid acid catalysts for alcohol dehydration, allowing us to explore the role of confinement separately to the nature of the acid site. In doing so, this will provide unique insights for future catalyst design for sustainable, bio-based processes.

ASSOCIATED CONTENT

Supporting Information

The Supporting Information is available free of charge at https://pubs.acs.org/doi/10.1021/acscatal.3c00352.

Coordinate files for calculated geometries for high-level quantum chemical calculations (TXT)

Further experimental methodology, characterization, catalysis, molecular dynamics, and high-level quantum chemical results (PDF)

https://doi.org/10.1021/acscatal.3c00352
ACS Catal. 2023, 13, 5955−5968

AUTHOR INFORMATION

Corresponding Author

Matthew E. Potter − *School of Chemistry, University of Southampton, Southampton, Hampshire SO17 1BJ, U.K.*; orcid.org/0000-0001-9849-3306; Email: M.E.Potter@soton.ac.uk

Authors

Jonas Amsler − *Institute of Catalysis Research and Technology, Karlsruhe Institute of Technology, 76344 Eggenstein-Leopoldshafen, Germany*; orcid.org/0000-0003-3112-4957

Lucas Spiske − *Institute of Catalysis Research and Technology, Karlsruhe Institute of Technology, 76344 Eggenstein-Leopoldshafen, Germany*

Philipp N. Plessow − *Institute of Catalysis Research and Technology, Karlsruhe Institute of Technology, 76344 Eggenstein-Leopoldshafen, Germany*

Theresah Asare − *School of Chemistry, University of Southampton, Southampton, Hampshire SO17 1BJ, U.K.*

Marina Carravetta − *School of Chemistry, University of Southampton, Southampton, Hampshire SO17 1BJ, U.K.*

Robert Raja − *School of Chemistry, University of Southampton, Southampton, Hampshire SO17 1BJ, U.K.*; orcid.org/0000-0002-4161-7053

Paul A. Cox − *School of Pharmacy and Biomedical Sciences, University of Portsmouth, Portsmouth PO1 2UP, U.K.*

Felix Studt − *Institute of Catalysis Research and Technology, Karlsruhe Institute of Technology, 76344 Eggenstein-Leopoldshafen, Germany; Institute for Chemical Technology and Polymer Chemistry, Karlsruhe Institute of Technology, 76131 Karlsruhe, Germany*; orcid.org/0000-0001-6841-4232

Lindsay-Marie Armstrong − *School of Engineering, University of Southampton, Southampton, Hampshire SO17 1BJ, U.K.*

Complete contact information is available at: https://pubs.acs.org/10.1021/acscatal.3c00352

Author Contributions

This manuscript was written through contributions of all authors. All authors have given approval to the final version of the manuscript.

Funding

The authors acknowledge the TotalEnergies "Consortium on Metal Nanocatalysis" project for funding. J.A., P.N.P., and F.S. gratefully acknowledge support from GRK 2450, by the state of Baden-Württemberg through bwHPC (bwUniCluster and JUSTUS, RV bw17D01), and by the Helmholtz Association.

Notes

The authors declare no competing financial interest.

REFERENCES

(1) Palkovits, R.; Delidovich, I. Efficient utilization of renewable feedstocks: the role of catalysis and process design. *Philos. Trans. R. Soc., A* **2018**, *376*, No. 20170064.

(2) Lange, J.-P. Performance metrics for sustainable catalysis in industry. *Nat. Catal.* **2021**, *4*, 186−192.

(3) Zhang, X.; Fevre, M.; Jones, G. O.; Waymouth, R. M. Catalysis as an Enabling Science for Sustainable Polymers. *Chem. Rev.* **2018**, *118*, 839−885.

(4) Mika, L. T.; Csefalvay, E.; Nemeth, A. Catalytic Conversion of Carbohydrates to Initial Platform Chemicals: Chemistry and Sustainability. *Chem. Rev.* **2018**, *118*, 505−613.

(5) Burkart, M. D.; Hazari, N.; Tway, C. L.; Zeitler, E. L. Opportunities and Challenges for Catalysis in Carbon Dioxide Utilization. *ACS Catal.* **2019**, *9*, 7937−7956.

(6) Bender, T. A.; Dabrowski, J. A.; Gagné, M. R. Homogeneous catalysis for the production of low-volume, high-value chemicals from biomass. *Nat. Rev. Chem.* **2018**, *2*, 35−46.

(7) Olah, G. A. Beyond oil and gas: the methanol economy. *Angew. Chem., Int. Ed.* **2005**, *44*, 2636−2639.

(8) Kember, M. R.; Buchard, A.; Williams, C. K. Catalysts for CO2/epoxide copolymerisation. *Chem. Commun.* **2011**, *47*, 141−163.

(9) Martin, O.; Martin, A. J.; Mondelli, C.; Mitchell, S.; Segawa, T. F.; Hauert, R.; Drouilly, C.; Curulla-Ferre, D.; Perez-Ramirez, J. Indium Oxide as a Superior Catalyst for Methanol Synthesis by CO2 Hydrogenation. *Angew. Chem., Int. Ed.* **2016**, *55*, 6261−6265.

(10) Kamkeng, A. D. N.; Wang, M.; Hu, J.; Du, W.; Qian, F. Transformation technologies for CO2 utilisation: Current status, challenges and future prospects. *Chem. Eng. J.* **2021**, *409*, No. 128138.

(11) Lee, W. J.; Li, C.; Prajitno, H.; Yoo, J.; Patel, J.; Yang, Y.; Lim, S. Recent trend in thermal catalytic low temperature CO2 methanation: A critical review. *Catal. Today* **2021**, *368*, 2−19.

(12) Lin, Y.-C.; Huber, G. W. The critical role of heterogeneous catalysis in lignocellulosic biomass conversion. *Energy Environ. Sci.* **2009**, *2*, 68−80.

(13) Rehman, A.; Noor, T.; Hussain, A.; Iqbal, N.; Jahan, Z. Role of Catalysis in Biofuels Production Process − A Review. *ChemBioEng Rev.* **2021**, *8*, 417−438.

(14) Grim, R. G.; To, A. T.; Farberow, C. A.; Hensley, J. E.; Ruddy, D. A.; Schaidle, J. A. Growing the Bioeconomy through Catalysis: A Review of Recent Advancements in the Production of Fuels and Chemicals from Syngas-Derived Oxygenates. *ACS Catal.* **2019**, *9*, 4145−4172.

(15) Wingad, R. L.; Gates, P. J.; Street, S. T. G.; Wass, D. F. Catalytic Conversion of Ethanol to n-Butanol Using Ruthenium P−N Ligand Complexes. *ACS Catal.* **2015**, *5*, 5822−5826.

(16) Osman, A. I.; Hefny, M.; Abdel Maksoud, M. I. A.; Elgarahy, A. M.; Rooney, D. W. Recent advances in carbon capture storage and utilisation technologies: a review. *Environ. Chem. Lett.* **2021**, *19*, 797−849.

(17) Saravanan, A.; Senthil kumar, P.; Vo, D.-V. N.; Jeevanantham, S.; Bhuvaneswari, V.; Anantha Narayanan, V.; Yaashikaa, P. R.; Swetha, S.; Reshma, B. A comprehensive review on different approaches for CO2 utilization and conversion pathways. *Chem. Eng. Sci.* **2021**, *236*, No. 116515.

(18) Hepburn, C.; Adlen, E.; Beddington, J.; Carter, E. A.; Fuss, S.; Mac Dowell, N.; Minx, J. C.; Smith, P.; Williams, C. K. The technological and economic prospects for CO2 utilization and removal. *Nature* **2019**, *575*, 87−97.

(19) Ethiraj, J.; Wagh, D.; Manyar, H. Advances in Upgrading Biomass to Biofuels and Oxygenated Fuel Additives Using Metal Oxide Catalysts. *Energy Fuels* **2022**, *36*, 1189−1204.

(20) Pattnaik, F.; Tripathi, S.; Patra, B. R.; Nanda, S.; Kumar, V.; Dalai, A. K.; Naik, S. Catalytic conversion of lignocellulosic polysaccharides to commodity biochemicals: a review. *Environ. Chem. Lett.* **2021**, *19*, 4119−4136.

(21) Zacharopoulou, V.; Lemonidou, A. Olefins from Biomass Intermediates: A Review. *Catalysts* **2018**, *8*, 2.

(22) Scotti, N.; Zaccheria, F.; Evangelisti, C.; Psaro, R.; Ravasio, N. Dehydrogenative coupling promoted by copper catalysts: a way to optimise and upgrade bio-alcohols. *Catal. Sci. Technol.* **2017**, *7*, 1386−1393.

(23) Palma, V.; Ruocco, C.; Cortese, M.; Martino, M. Bioalcohol Reforming: An Overview of the Recent Advances for the Enhancement of Catalyst Stability. *Catalysts* **2020**, *10*, 665.

(24) Walther, T.; Francois, J. M. Microbial production of propanol. *Biotechnol. Adv.* **2016**, *34*, 984−996.

(25) Galadima, A.; Muraza, O. Catalytic Upgrading of Bioethanol to Fuel Grade Biobutanol: A Review. *Ind. Eng. Chem. Res.* **2015**, *54*, 7181−7194.

(26) Pinaeva, L.; Noskov, A. Potentials of bio-butanol conversion to valuable products. *Rev. Chem. Eng.* **2022**, DOI: 10.1515/revce-2021-0066.
(27) Liu, X.; Yu, X. Enhancement of Butanol Production: From Biocatalysis to Bioelectrocatalysis. *ACS Energy Lett.* **2020**, *5*, 867−878.
(28) Lepore, A. W.; Li, Z.; Davison, B. H.; Foo, G. S.; Wu, Z.; Narula, C. K. Catalytic Dehydration of Biomass Derived 1-Propanol to Propene over M-ZSM-5 (M = H, V, Cu, or Zn). *Ind. Eng. Chem. Res.* **2017**, *56*, 4302−4308.
(29) Zhi, Y.; Shi, H.; Mu, L.; Liu, Y.; Mei, D.; Camaioni, D. M.; Lercher, J. A. Dehydration Pathways of 1-Propanol on HZSM-5 in the Presence and Absence of Water. *J. Am. Chem. Soc.* **2015**, *137*, 15781−15794.
(30) Pfriem, N.; Hintermeier, P. H.; Eckstein, S.; Kim, S.; Liu, Q.; Shi, H.; Milakovic, L.; Liu, Y.; Haller, G. L.; Barath, E.; Liu, Y.; Lercher, J. A. Role of the ionic environment in enhancing the activity of reacting molecules in zeolite pores. *Science* **2021**, *372*, 952−957.
(31) Chowdhury, A. D.; Lucini Paioni, A.; Whiting, G. T.; Fu, D.; Baldus, M.; Weckhuysen, B. M. Unraveling the Homologation Reaction Sequence of the Zeolite-Catalyzed Ethanol-to-Hydrocarbons Process. *Angew. Chem., Int. Ed.* **2019**, *58*, 3908−3912.
(32) Soh, J. C.; Chong, S. L.; Hossain, S. S.; Cheng, C. K. Catalytic ethylene production from ethanol dehydration over non-modified and phosphoric acid modified Zeolite H-Y (80) catalysts. *Fuel Process. Technol.* **2017**, *158*, 85−95.
(33) Kamsuwan, T.; Jongsomjit, B. A Comparative Study of Different Al-based Solid Acid Catalysts for Catalytic Dehydration of Ethanol. *Eng. J.* **2016**, *20*, 63−75.
(34) Yin, J.; Guo, X.; Sun, Y.; Han, S.; Li, Q. Understanding the Nanoconfinement Effect on the Ethanol-to-Propene Mechanism Catalyzed by Acidic ZSM-5 and FAU Zeolites. *J. Phys. Chem. C* **2021**, *125*, 310−334.
(35) Gołąbek, K.; Tarach, K. A.; Filek, U.; Gora-Marek, K. Ethylene formation by dehydration of ethanol over medium pore zeolites. *Spectrochim. Acta, Part A* **2018**, *192*, 464−472.
(36) Müller, J. M.; Mesquita, G. C.; Franco, S. M.; Borges, L. D.; de Macedo, J. L.; Dias, J. A.; Dias, S. C. L. Solid-state dealumination of zeolites for use as catalysts in alcohol dehydration. *Microporous Mesoporous Mater.* **2015**, *204*, 50−57.
(37) Wu, C. Y.; Wu, H. S. Ethylene Formation from Ethanol Dehydration Using ZSM-5 Catalyst. *ACS Omega* **2017**, *2*, 4287−4296.
(38) Phung, T. K.; Proietti Hernández, L.; Lagazzo, A.; Busca, G. Dehydration of ethanol over zeolites, silica alumina and alumina: Lewis acidity, Brønsted acidity and confinement effects. *Appl. Catal., A* **2015**, *493*, 77−89.
(39) Phung, T. K.; Lagazzo, A.; Rivero Crespo, M. Á.; Sánchez Escribano, V.; Busca, G. A study of commercial transition aluminas and of their catalytic activity in the dehydration of ethanol. *J. Catal.* **2014**, *311*, 102−113.
(40) Christiansen, M. A.; Mpourmpakis, G.; Vlachos, D. G. DFT-driven multi-site microkinetic modeling of ethanol conversion to ethylene and diethyl ether on γ-Al2O3(1 1 1). *J. Catal.* **2015**, *323*, 121−131.
(41) Feng, R.; Hu, X.; Yan, X.; Yan, Z.; Rood, M. J. A high surface area mesoporous γ-Al2O3 with tailoring texture by glucose template for ethanol dehydration to ethylene. *Microporous Mesoporous Mater.* **2017**, *241*, 89−97.
(42) DeWilde, J. F.; Chiang, H.; Hickman, D. A.; Ho, C. R.; Bhan, A. Kinetics and Mechanism of Ethanol Dehydration on γ-Al2O3: The Critical Role of Dimer Inhibition. *ACS Catal.* **2013**, *3*, 798−807.
(43) Ferri, P.; Li, C.; Millán, R.; Martínez-Triguero, J.; Moliner, M.; Boronat, M.; Corma, A. Impact of Zeolite Framework Composition and Flexibility on Methanol-To-Olefins Selectivity: Confinement or Diffusion? *Angew. Chem.* **2020**, *132*, 19876−19883.
(44) Potter, M. E. Down the Microporous Rabbit Hole of Silicoaluminophosphates: Recent Developments on Synthesis, Characterization, and Catalytic Applications. *ACS Catal.* **2020**, *10*, 9758−9789.
(45) Jae, J.; Tompsett, G. A.; Foster, A. J.; Hammond, K. D.; Auerbach, S. M.; Lobo, R. F.; Huber, G. W. Investigation into the shape selectivity of zeolite catalysts for biomass conversion. *J. Catal.* **2011**, *279*, 257−268.
(46) Olsbye, U.; Svelle, S.; Bjorgen, M.; Beato, P.; Janssens, T. V.; Joensen, F.; Bordiga, S.; Lillerud, K. P. Conversion of methanol to hydrocarbons: how zeolite cavity and pore size controls product selectivity. *Angew. Chem., Int. Ed.* **2012**, *51*, 5810−5831.
(47) Grifoni, E.; Piccini, G.; Lercher, J. A.; Glezakou, V. A.; Rousseau, R.; Parrinello, M. Confinement effects and acid strength in zeolites. *Nat. Commun.* **2021**, *12*, No. 2630.
(48) Cnudde, P.; Demuynck, R.; Vandenbrande, S.; Waroquier, M.; Sastre, G.; Speybroeck, V. V. Light Olefin Diffusion during the MTO Process on H-SAPO-34: A Complex Interplay of Molecular Factors. *J. Am. Chem. Soc.* **2020**, *142*, 6007−6017.
(49) Bingre, R.; Louis, B.; Nguyen, P. An Overview on Zeolite Shaping Technology and Solutions to Overcome Diffusion Limitations. *Catalysts* **2018**, *8*, 163.
(50) Bhan, A.; Iglesia, E. A link between reactivity and local structure in acid catalysis on zeolites. *Acc. Chem. Res.* **2008**, *41*, 559−567.
(51) Thomas, J. M.; Raja, R.; Sankar, G.; Bell, R. G. Molecular-sieve catalysts for the selective oxidation of linear alkanes by molecular oxygen. *Nature* **1999**, *398*, 227−230.
(52) O'Malley, A. J.; Garcia Sakai, V.; Silverwood, I. P.; Dimitratos, N.; Parker, S. F.; Catlow, C. R. Methanol diffusion in zeolite HY: a combined quasielastic neutron scattering and molecular dynamics simulation study. *Phys. Chem. Chem. Phys.* **2016**, *18*, 17294−17302.
(53) Potter, M. E.; O'Malley, A. J.; Chapman, S.; Kezina, J.; Newland, S. H.; Silverwood, I. P.; Mukhopadhyay, S.; Carravetta, M.; Mezza, T. M.; Parker, S. F.; Catlow, C. R. A.; Raja, R. Understanding the Role of Molecular Diffusion and Catalytic Selectivity in Liquid-Phase Beckmann Rearrangement. *ACS Catal.* **2017**, *7*, 2926−2934.
(54) Kadam, S. A.; Shamzhy, M. V. IR Operando study of ethanol dehydration over MFI zeolite. *Catal. Today* **2018**, *304*, 51−57.
(55) Zhou, X.; Wang, C.; Chu, Y.; Xu, J.; Wang, Q.; Qi, G.; Zhao, X.; Feng, N.; Deng, F. Observation of an oxonium ion intermediate in ethanol dehydration to ethene on zeolite. *Nat. Commun.* **2019**, *10*, No. 1961.
(56) Zeng, S.; Li, J.; Wang, N.; Zhang, W.; Wei, Y.; Liu, Z.; Xu, S. Investigation of Ethanol Conversion on H-ZSM-5 Zeolite by in Situ Solid-State NMR. *Energy Fuels* **2021**, *35*, 12319−12328.
(57) Aramburo, L. R.; de Smit, E.; Arstad, B.; van Schooneveld, M. M.; Sommer, L.; Juhin, A.; Yokosawa, T.; Zandbergen, H. W.; Olsbye, U.; de Groot, F. M.; Weckhuysen, B. M. X-ray imaging of zeolite particles at the nanoscale: influence of steaming on the state of aluminum and the methanol-to-olefin reaction. *Angew. Chem., Int. Ed.* **2012**, *51*, 3616−3619.
(58) Qian, Q.; Ruiz-Martínez, J.; Mokhtar, M.; Asiri, A. M.; Al-Thabaiti, S. A.; Basahel, S. N.; Weckhuysen, B. M. Single-catalyst particle spectroscopy of alcohol-to-olefins conversions: Comparison between SAPO-34 and SSZ-13. *Catal. Today* **2014**, *226*, 14−24.
(59) Miletto, I.; Paul, G.; Chapman, S.; Gatti, G.; Marchese, L.; Raja, R.; Gianotti, E. Mesoporous Silica Scaffolds as Precursor to Drive the Formation of Hierarchical SAPO-34 with Tunable Acid Properties. *Chem. − Eur. J.* **2017**, *23*, 9952−9961.
(60) Pérez-Ramírez, J.; Christensen, C. H.; Egeblad, K.; Christensen, C. H.; Groen, J. C. Hierarchical zeolites: enhanced utilisation of microporous crystals in catalysis by advances in materials design. *Chem. Soc. Rev.* **2008**, *37*, 2530−2542.
(61) Hartmann, M.; Kevan, L. Substitution of transition metal ions into aluminophosphates and silicoaluminophosphates: characterization and relation to catalysis. *Res. Chem. Intermed.* **2002**, *28*, 625−695.
(62) Chen, J. Q.; Bozzano, A.; Glover, B.; Fuglerud, T.; Kvisle, S. Recent advancements in ethylene and propylene production using the UOP/Hydro MTO process. *Catal. Today* **2005**, *106*, 103−107.
(63) Gogate, M. R. Methanol-to-olefins process technology: current status and future prospects. *Petrol. Sci. Technol.* **2019**, *37*, 559−565.

(64) Huo, H.; Peng, L.; Gan, Z.; Grey, C. P. Solid-state MAS NMR studies of Bronsted acid sites in zeolite H-Mordenite. *J. Am. Chem. Soc.* **2012**, *134*, 9708−9720.
(65) Yokoi, T.; Mochizuki, H.; Namba, S.; Kondo, J. N.; Tatsumi, T. Control of the Al Distribution in the Framework of ZSM-5 Zeolite and Its Evaluation by Solid-State NMR Technique and Catalytic Properties. *J. Phys. Chem. C* **2015**, *119*, 15303−15315.
(66) Potter, M. E.; Armstrong, L.-M.; Raja, R. Combining catalysis and computational fluid dynamics towards improved process design for ethanol dehydration. *Catal. Sci. Technol.* **2018**, *8*, 6163−6172.
(67) Potter, M. E.; Cholerton, M. E.; Kezina, J.; Bounds, R.; Carravetta, M.; Manzoli, M.; Gianotti, E.; Lefenfeld, M.; Raja, R. Role of Isolated Acid Sites and Influence of Pore Diameter in the Low-Temperature Dehydration of Ethanol. *ACS Catal.* **2014**, *4*, 4161−4169.
(68) Alexopoulos, K.; John, M.; Van der Borght, K.; Galvita, V.; Reyniers, M.-F.; Marin, G. B. DFT-based microkinetic modeling of ethanol dehydration in H-ZSM-5. *J. Catal.* **2016**, *339*, 173−185.
(69) John, M.; Alexopoulos, K.; Reyniers, M.-F.; Marin, G. B. First-Principles Kinetic Study on the Effect of the Zeolite Framework on 1-Butanol Dehydration. *ACS Catal.* **2016**, *6*, 4081−4094.
(70) Potter, M. E.; Aswegen, S. V.; Gibson, E. K.; Silverwood, I. P.; Raja, R. Spectroscopic investigation into the design of solid-acid catalysts for the low temperature dehydration of ethanol. *Phys. Chem. Chem. Phys.* **2016**, *18*, 17303−17310.
(71) Konda, S. S. M.; Caratzoulas, S.; Vlachos, D. G. Computational Insights into the Role of Metal and Acid Sites in Bifunctional Metal/Zeolite Catalysts: A Case Study of Acetone Hydrogenation to 2-Propanol and Subsequent Dehydration to Propene. *ACS Catal.* **2016**, *6*, 123−133.
(72) Amsler, J.; Bernart, S.; Plessow, P. N.; Studt, F. Theoretical investigation of the olefin cycle in H-SSZ-13 for the ethanol-to-olefins process using ab initio calculations and kinetic modeling. *Catal. Sci. Technol.* **2022**, *12*, 3311−3321.
(73) Kim, S.; Robichaud, D. J.; Beckham, G. T.; Paton, R. S.; Nimlos, M. R. Ethanol dehydration in HZSM-5 studied by density functional theory: evidence for a concerted process. *J. Phys. Chem. A* **2015**, *119*, 3604−3614.
(74) Prestianni, A.; Cortese, R.; Duca, D. Propan-2-ol dehydration on H-ZSM-5 and H-Y zeolite: a DFT study. *React. Kinet., Mech. Catal.* **2013**, *108*, 565−582.
(75) Alexopoulos, K.; Lee, M.-S.; Liu, Y.; Zhi, Y.; Liu, Y.; Reyniers, M.-F.; Marin, G. B.; Glezakou, V.-A.; Rousseau, R.; Lercher, J. A. Anharmonicity and Confinement in Zeolites: Structure, Spectroscopy, and Adsorption Free Energy of Ethanol in H-ZSM-5. *J. Phys. Chem. C* **2016**, *120*, 7172−7182.
(76) Piccini, G.; Alessio, M.; Sauer, J. Ab initio study of methanol and ethanol adsorption on Brønsted sites in zeolite H-MFI. *Phys. Chem. Chem. Phys.* **2018**, *20*, 19964−19970.
(77) Perdew, J. P.; Burke, K.; Ernzerhof, M. Generalized Gradient Approximation Made Simple. *Phys. Rev. Lett.* **1996**, *77*, 3865−3868.
(78) Grimme, S.; Antony, J.; Ehrlich, S.; Krieg, H. A consistent and accurate ab initio parametrization of density functional dispersion correction (DFT-D) for the 94 elements H-Pu. *J. Chem. Phys.* **2010**, *132*, No. 154104.
(79) Blöchl, P. E. Projector augmented-wave method. *Phys. Rev. B* **1994**, *50*, 17953−17979.
(80) Kresse, G.; Furthmuller, J. Efficient iterative schemes for ab initio total-energy calculations using a plane-wave basis set. *Phys. Rev. B* **1996**, *54*, 11169−11186.
(81) Kresse, G.; Joubert, D. From ultrasoft pseudopotentials to the projector augmented-wave method. *Phys. Rev. B: Condens. Matter Mater. Phys.* **1999**, *59*, 1758−1775.
(82) Monkhorst, H. J.; Pack, J. D. Special points for Brillouin-zone integrations. *Phys. Rev. B: Condens. Matter Mater. Phys.* **1976**, *13*, 5188−5192.
(83) Plessow, P. N. Efficient Transition State Optimization of Periodic Structures through Automated Relaxed Potential Energy Surface Scans. *J. Chem. Theory Comput.* **2018**, *14*, 981−990.
(84) Brogaard, R. Y.; Henry, R.; Schuurman, Y.; Medford, A. J.; Moses, P. G.; Beato, P.; Svelle, S.; Nørskov, J. K.; Olsbye, U. Methanol-to-hydrocarbons conversion: The alkene methylation pathway. *J. Catal.* **2014**, *314*, 159−169.
(85) Hansen, N.; Kerber, T.; Sauer, J.; Bell, A. T.; Keil, F. J. Quantum chemical modeling of benzene ethylation over H-ZSM-5 approaching chemical accuracy: a hybrid MP2:DFT study. *J. Am. Chem. Soc.* **2010**, *132*, 11525−11538.
(86) Ren, Q.; Rybicki, M.; Sauer, J. Interaction of C3−C5 Alkenes with Zeolitic Brønsted Sites: π-Complexes, Alkoxides, and Carbenium Ions in H-FER. *J. Phys. Chem. C* **2020**, *124*, 10067−10078.
(87) Rybicki, M.; Sauer, J. Ab Initio Prediction of Proton Exchange Barriers for Alkanes at Bronsted Sites of Zeolite H-MFI. *J. Am. Chem. Soc.* **2018**, *140*, 18151−18161.
(88) Svelle, S.; Tuma, C.; Rozanska, X.; Kerber, T.; Sauer, J. Quantum chemical modeling of zeolite-catalyzed methylation reactions: toward chemical accuracy for barriers. *J. Am. Chem. Soc.* **2009**, *131*, 816−825.
(89) Tuma, C.; Kerber, T.; Sauer, J. The tert-butyl cation in H-zeolites: deprotonation to isobutene and conversion into surface alkoxides. *Angew. Chem., Int. Ed.* **2010**, *49*, 4678−4680.
(90) Tuma, C.; Sauer, J. Treating dispersion effects in extended systems by hybrid MP2:DFT calculations–protonation of isobutene in zeolite ferrierite. *Phys. Chem. Chem. Phys.* **2006**, *8*, 3955−3965.
(91) Riplinger, C.; Neese, F. An efficient and near linear scaling pair natural orbital based local coupled cluster method. *J. Chem. Phys.* **2013**, *138*, No. 034106.
(92) Riplinger, C.; Sandhoefer, B.; Hansen, A.; Neese, F. Natural triple excitations in local coupled cluster calculations with pair natural orbitals. *J. Chem. Phys.* **2013**, *139*, No. 134101.
(93) Riplinger, C.; Pinski, P.; Becker, U.; Valeev, E. F.; Neese, F. Sparse maps–A systematic infrastructure for reduced-scaling electronic structure methods. II. Linear scaling domain based pair natural orbital coupled cluster theory. *J. Chem. Phys.* **2016**, *144*, No. 024109.
(94) Plessow, P. N.; Studt, F. Unraveling the Mechanism of the Initiation Reaction of the Methanol to Olefins Process Using ab Initio and DFT Calculations. *ACS Catal.* **2017**, *7*, 7987−7994.
(95) Goncalves, T. J.; Plessow, P. N.; Studt, F. On the Accuracy of Density Functional Theory in Zeolite Catalysis. *ChemCatChem* **2019**, *11*, 4368−4376.
(96) Feller, D. Application of systematic sequences of wave functions to the water dimer. *J. Chem. Phys.* **1992**, *96*, 6104−6114.
(97) Helgaker, T.; Klopper, W.; Koch, H.; Noga, J. Basis-set convergence of correlated calculations on water. *J. Chem. Phys.* **1997**, *106*, 9639−9646.
(98) Neese, F. Software update: the ORCA program system, version 4.0. *Wiley Interdiscip. Rev.: Comput. Mol. Sci.* **2017**, *8*, No. e1327.
(99) Neese, F. The ORCA program system. *Wiley Interdiscip. Rev.: Comput. Mol. Sci.* **2012**, *2*, 73−78.
(100) Janssen, C. L.; Nielsen, I. M. B. New diagnostics for coupled-cluster and Møller−Plesset perturbation theory. *Chem. Phys. Lett.* **1998**, *290*, 423−430.
(101) Weigend, F.; Häser, M.; Patzelt, H.; Ahlrichs, R. RI-MP2: optimized auxiliary basis sets and demonstration of efficiency. *Chem. Phys. Lett.* **1998**, *294*, 143−152.
(102) Jiang, W.; DeYonker, N. J.; Wilson, A. K. Multireference Character for 3d Transition-Metal-Containing Molecules. *J. Chem. Theory Comput.* **2012**, *8*, 460−468.
(103) Dunning, T. H. Gaussian basis sets for use in correlated molecular calculations. I. The atoms boron through neon and hydrogen. *J. Chem. Phys.* **1989**, *90*, 1007−1023.
(104) Minenkov, Y.; Chermak, E.; Cavallo, L. Accuracy of DLPNO-CCSD(T) method for noncovalent bond dissociation enthalpies from coinage metal cation complexes. *J. Chem. Theory Comput.* **2015**, *11*, 4664−4676.
(105) Minenkov, Y.; Bistoni, G.; Riplinger, C.; Auer, A. A.; Neese, F.; Cavallo, L. Pair natural orbital and canonical coupled cluster reaction enthalpies involving light to heavy alkali and alkaline earth

https://doi.org/10.1021/acscatal.3c00352
ACS Catal. 2023, 13, 5955−5968

metals: the importance of sub-valence correlation. *Phys. Chem. Chem. Phys.* **2017**, *19*, 9374−9391.
(106) Saitow, M.; Becker, U.; Riplinger, C.; Valeev, E. F.; Neese, F. A new near-linear scaling, efficient and accurate, open-shell domain-based local pair natural orbital coupled cluster singles and doubles theory. *J. Chem. Phys.* **2017**, *146*, No. 164105.
(107) Neese, F.; Wennmohs, F.; Hansen, A.; Becker, U. Efficient, approximate and parallel Hartree−Fock and hybrid DFT calculations. A 'chain-of-spheres' algorithm for the Hartree−Fock exchange. *Chem. Phys.* **2009**, *356*, 98−109.
(108) Hjorth Larsen, A.; Jorgen Mortensen, J.; Blomqvist, J.; Castelli, I. E.; Christensen, R.; Dulak, M.; Friis, J.; Groves, M. N.; Hammer, B.; Hargus, C.; Hermes, E. D.; Jennings, P. C.; Bjerre Jensen, P.; Kermode, J.; Kitchin, J. R.; Leonhard Kolsbjerg, E.; Kubal, J.; Kaasbjerg, K.; Lysgaard, S.; Bergmann Maronsson, J.; Maxson, T.; Olsen, T.; Pastewka, L.; Peterson, A.; Rostgaard, C.; Schiotz, J.; Schutt, O.; Strange, M.; Thygesen, K. S.; Vegge, T.; Vilhelmsen, L.; Walter, M.; Zeng, Z.; Jacobsen, K. W. The atomic simulation environment-a Python library for working with atoms. *J. Phys.: Condens. Matter* **2017**, *29*, 273002.
(109) Sun, H. COMPASS: An ab Initio Force-Field Optimized for Condensed-Phase Applications Overview with Details on Alkane and Benzene Compounds. *J. Phys. Chem. B* **1998**, *102*, 7338−7364.
(110) Biovia, D. S. Materials Studio. *R2 (Dassault Systèmes BIOVIA*, San Diego, 2017.
(111) Deutschmann, O. T. S.; Correa, C.; Chatterjee, D.; Kleditzsch, S.; Janardhanan, V. M.; Mladenov, N.; Minh, H. D.; Karadeniz, H.; Hettel, M.; Menon, V.; Banerjee, A.; Gossler, H.; Shisath, A.; Daymo, E. *DETCHEM Software package, 2.9 ed.* www.detchem.com, Karlsruhe, 2022.
(112) Potter, M. E.; Kezina, J.; Bounds, R.; Carravetta, M.; Mezza, T. M.; Raja, R. Investigating the role of framework topology and accessible active sites in silicoaluminophosphates for modulating acid-catalysis. *Catal. Sci. Technol.* **2018**, *8*, 5155−5164.
(113) Al-Faze, R.; Kozhevnikova, E. F.; Kozhevnikov, I. V. Diethyl Ether Conversion to Ethene and Ethanol Catalyzed by Heteropoly Acids. *ACS Omega* **2021**, *6*, 9310−9318.
(114) Kyrimis, S.; Rankin, K. E.; Potter, M. E.; Raja, R.; Armstrong, L.-M. Towards realistic characterisation of chemical reactors: An in-depth analysis of catalytic particle beds produced by sieving. *Adv. Powder Technol.* **2023**, *34*, No. 103932.
(115) de las Pozas, C.; Lopez-Cordero, R.; Gonzalez-Morales, J. A.; Travieso, N.; Roque-Malherbe, R. Effect of pore diameter and acid strength in ethanol dehydration on molecular sieves. *J. Mol. Catal.* **1993**, *83*, 145−156.
(116) Roy, S.; Mpourmpakis, G.; Hong, D.-Y.; Vlachos, D. G.; Bhan, A.; Gorte, R. J. Mechanistic Study of Alcohol Dehydration on γ-Al2O3. *ACS Catal.* **2012**, *2*, 1846−1853.
(117) Plessow, P. N.; Studt, F. Theoretical Insights into the Effect of the Framework on the Initiation Mechanism of the MTO Process. *Catal. Lett.* **2018**, *148*, 1246−1253.
(118) Gunst, D.; Alexopoulos, K.; Van Der Borght, K.; John, M.; Galvita, V.; Reyniers, M.-F.; Verberckmoes, A. Study of butanol conversion to butenes over H-ZSM-5: Effect of chemical structure on activity, selectivity and reaction pathways. *Appl. Catal., A* **2017**, *539*, 1−12.

https://doi.org/10.1021/acscatal.3c00352
ACS Catal. 2023, 13, 5955−5968